# Steam oxidation properties of Graphene reinforced bioinspired laminated CoCrFeNiMn high-entropy alloy matrix composites at 1000 ℃

*Chongyang Liu[a,b], Xiaosong Jiang[a,b*], Hongliang Sun[a,b], Tianyan Liuc*, Zixuan Wd[c], Liu Yang[e]*

*[a] Key Laboratory of Advanced Technologies of Materials, Ministry of Education, Chengdu 610031, China*

*[b] School of Materials Science and Engineering, Southwest Jiaotong University, Chengdu Sichuan 610031, China*

*[c]Reactor Engineering Research Sub-institute, Nuclear Power Institute of China, Chengdu 610005, People's Republic of China*

*[d] School of Engineering and Materials Science, Queen Mary University of London, London E1 4NS, United Kingdom*

*[e] Institute for Applied Materials (IAM-WK), Karlsruhe Institute of Technology (KIT), Karlsruhe 76131, Germany*

***Corresponding author**: xsjiang@swjtu.edu.cn (X.S. Jiang) OR rexroi@hotmail.com (T.Y. Liu).*

**Abstract:** Laminated CoCrFeNiMn high-entropy alloy (HEA) matrix composites reinforced with 1.0 wt. % graphene nanoplatelets (GNPs) were fabricated by mechanical ball milling and flake powder metallurgy, and were isothermal oxidized at 1000℃ for 100h. Vacuum hot-pressure sintering (VHPS) shows a distinct nacre structure with the microstructure composed of FCC matrix phase, $Cr_{23}C_6$, $CrMn_{1.5}O_4$ precipitated phases, numerous dislocations and twins. High-temperature oxidation tests showed that the composites had mass gains at 12h intervals from 12 to 100 h respectively. The oxidation kinetic curve changes from a linear pattern in the early stages to an exponential pattern in the later stages, which demonstrates better long-term oxidation resistance. The anisotropy of the laminated structure results in excellent resistance to

high-temperature steam oxidation in the vertical lamellar direction. Observation of the cross-section reveals that although $Cr_2O_3$ (inner layer) is present, $(Mn, Cr)_3O_4$ and $Mn_3O_4$ are the dominant oxides (outer layer). Elemental depletion zones for Mn and Cr exist in the region of the matrix near the oxide scales. The results show that the oxidation resistance of the laminated GNPs/CoCrFeNiMn composites is mainly influenced by the diffusion of Mn and Cr elements, the microstructure of the laminations and the internal oxidation.

**Keywords**: Bio-inspired laminates; High-entropy alloy matrix composites; Microstructure; Steam oxidation; Oxidation mechanisms

## 1 Introduction

Nowadays, under the requirement of increasing working temperature and pressure, advanced structural materials with excellent mechanical strength and high-temperature corrosion resistance are required [1, 2]. In contrast to conventional alloys, HEAs maintain stable random solid-solution phase [3], excellent mechanical properties [4], corrosion resistant at room and high temperatures [5], and good toughness at low temperatures [6]. Cantor alloys (iso-atomic, single-phase solid solutions of CoCrFeNiMn are an important HEAs system [7]. The FCC solid solution has a simple single-phase structure with good resistance to high-temperature softening, forging properties and low temperature yield strength [8-11]. The higher activation energy for oxygen diffusion and the higher vacancy mobility in HEAs show better resistance to oxidation and radiation than in conventional alloys [12, 13]. There are various ways to improve the strength of HEAs, such as plastic deformation, grain refinement and the addition of precipitating agents, etc [14, 15].

In recent years, inspired by nature's biomaterial hierarchies and their associated multi-scale toughening mechanisms [16], novel biomimetic structures have been widely used in the research of HEAs performance enhancement. The nacreous lamellar structure is better known in biomaterials [17, 18]. Graphene nanoplatelets have a large specific surface area, which ensures that the carbon nanoplatelets are aligned parallel along the horizontal direction. And it

forms a strong interface with the metal matrix, which fully exploits its load-bearing capacity [19-21]. S. Guan et al. [22] additive fabricated a CoCrFeNiMn/AlCoCrFeNi$Ti_{0.5}$ laminate HEAs that exhibited strength-plasticity synergy. Y. Yang et al. [23] similarly prepared laminated composites consisting of 304L stainless steel and CoCrFeNiMn HEA by additive manufacturing and achieved excellent overall mechanical properties. C. Shu et al. [24] synthesized biomimetic microlaminated TiC-CoCrCuFeNi composites with excellent mechanical properties and wear resistance.

So far, the high-temperature oxidation properties of HEAs in high-temperature corrosive environments have also received much attention [25-27]. HEAs reduce oxidation by virtue of their low diffusion coefficients, high element concentrations and complex composition combinations, enhancing the oxidation resistance [28-30]. The oxidation of CoCrFeNiMn HEAs at atmospheric pressure results in the formation of a laminar oxide film, which consists of an internal oxide rich in Cr and an external oxide rich in Mn [31, 32]. The main reason for this is the outward diffusion of metal cations, especially the high mobility and low production energy of the Mn element, which has a great influence on the oxidation resistance [33-36]. The diffusion of metallic elements to the interface leads to depletion of the elements in the internal region and improves the oxidation resistance to some extent [37]. The oxidation behavior of Cr-rich alloys (e.g. stainless steels and nickel-based alloys) can be affected by water steam. The addition of Mn affects the growth rate of the oxide scales [38, 39]. G.R. Holcomb et al. [32] also emphasized that future work should strengthen the analysis at the early stages of oxidation to verify whether protective oxides are formed at an early stage. Comparative studies of the oxidation mechanisms, oxidation kinetics and degradation behavior of HEAs in dry and humid environments are scarce [25].

In this paper, graphene-reinforced nacreous laminated CoCrFeNiMn HEA matrix composites were successfully synthesized by mechanical ball milling and microstructure design method for flake powder metallurgy. In previous work [40], the results showed that the laminated structure can achieve strength-plasticity synergy. In this work, the laminated composites were subjected to 100 h of isothermal water steam oxidation at 1000 ℃. The short-term and long-

term oxidation kinetic curves of the composites were analyzed, and the mechanism of oxidation of nacreous laminates, HEAs and graphene to high-temperature water vapor was studied in depth using X-ray diffraction, scanning electron microscopy and transmission electron microscopy.

## 2 Materials and methods

### 2.1 Materials

The high entropy alloy powders were pre-alloyed powders with an iso-atomic ratio of 45-105 μm particle size. Graphene nanoplatelets (GNPs) have a sheet diameter of 7-12 μm and a specific surface area of 50-200 $m^2/g$. Using rutin to graft hydrophilic groups on the surface of GNPs to improve its dispersion. The powder slurry of GNPs (1.0 wt.%) mixed with flake high entropy alloy powder was prepared by mechanical ball milling in a planetary ball mill with a ball to material ratio of 20:1 and a rotational speed of 300 rpm for 11 h. GNPs were added and ball milling continued for 1 h. The powder slurry of GNPs mixed with flake high entropy alloy powder was prepared. The ball-milled slurry mixture was frozen in the vacuum freeze-dryer (FD-a-50) for 24h to remove the protective medium (tert-butanol). Vacuum hot-pressure sintering (VHPS) was used to prepare GNPs reinforced laminated CoCrFeNiMn high-entropy alloy matrix composites. Sintering temperature is 1000 ℃, heating rate 10 ℃/min. The temperature was gradually pressurized to 35MPa during the heating process, followed by holding for 1h and cooling with the furnace. The process flow diagram is shown in Figure 1.

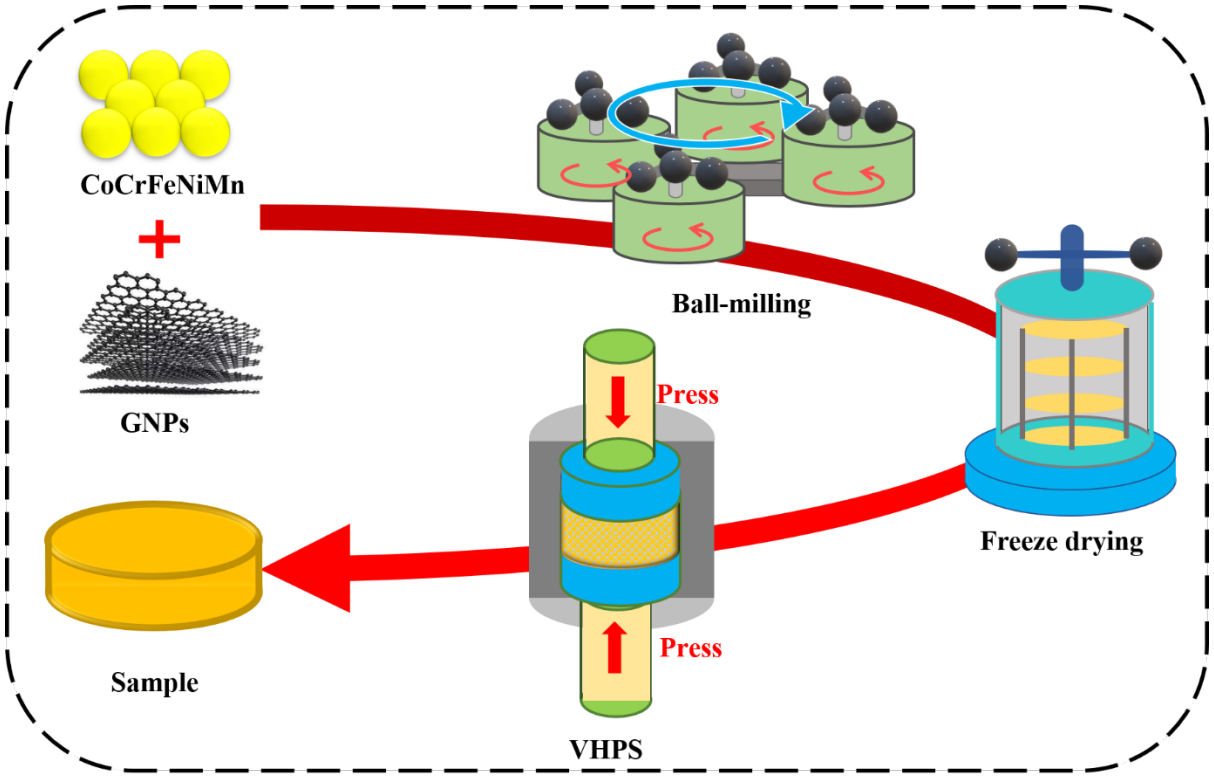


Figure 1. Schematic diagram of the preparation process of laminated GNPs/CoCrFeNiMn HEA matrix composites.

2.2 High-temperature Steam Oxidation Test

The blocks prepared by sintering were cut out in 5x5x10 mm samples and sequentially ground fine to 1500 mesh using SiC sandpaper. The samples were then polished to a mirror finish with a W2.5 diamond polishing paste, ultrasonically cleaned using acetone and dried in air. The oxidation experiments were done under a high-temperature water steam oxidation oven (as in Figure 2) for 100 h at 1000 ℃. Weighing was carried out every 12 h using an electronic balance with an accuracy of 0.01 mg.

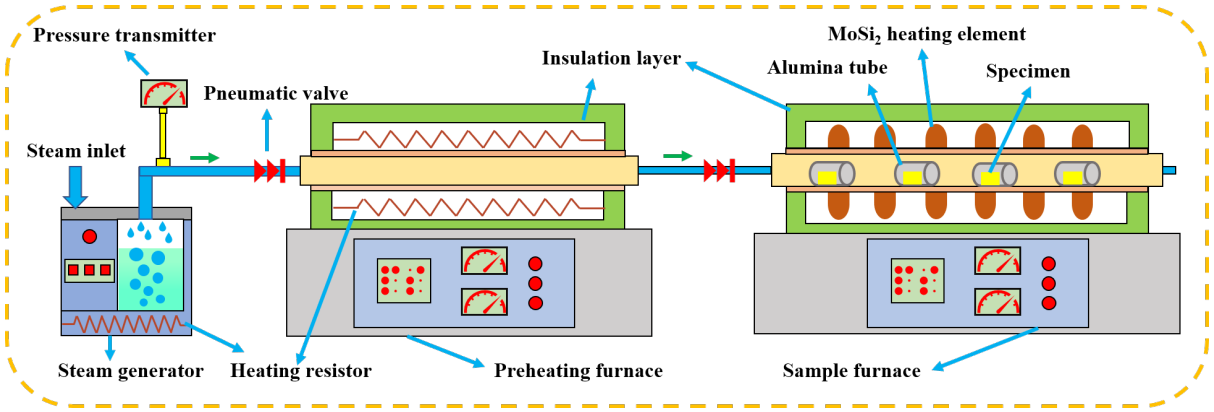

Figure 2. Schematic diagram of the high-temperature water vapor furnace.

2.3 Characterization

Cu-Kα radiation X-ray diffraction (XRD, X. Pert Pro-MPD) was used to analyze the phase composition of the composites after oxidation at high temperatures, which was scanned over a 2θ range from 10 ° to 90 ° with a step width of 0.02 °. The surface morphology after oxidation was analyzed by scanning electron microscopy (SEM, ZEISS Gemini 300) and the oxide composition of the composites was analyzed locally by energy dispersive spectrometer (EDS, Smartedx). The microstructure of the composites was characterized using transmission electron microscopy (TEM, FEI Tecnai F30) with selected area electron diffraction (SAED).

## 3 Results and discussion

3.1 Original structure and Phase

Mechanical ball milling enables the HEA powder to be broken down from the initial spherical particles to flake particles. The flakes of HEA powder made by ball milling are thoroughly mixed with GNPs. During the pressing of the raw material into the mold, the HEA flakes are aligned in a certain direction due to the force of gravity, resulting in laminated structures [41]. After powder metallurgy sintering HEA matrix composites with a laminated structure are formed, as shown in Figure 3. As shown in Figure 3(c), the HEA particles act as the "bricks", and the broken alloy particles and GNPs form the "slurry", which together form the nacreous laminate structure. The SEM images of the cross-section show the presence of two second phases in the microstructure, which were examined separately by EDS. The results show that the C-rich, Cr-rich phase is uniformly distributed and the O-rich, Cr-rich and Mn-rich phases are distributed between the "brick" layers. The oxidation of CoCrFeMnNi produces predominantly oxides of Mn and Cr rather than oxides of Fe, Co, and Ni, as the Gibbs free energy of the former is more negative than that of the latter [36]. During the experiment, the powder surface inevitably contacted with air, where Mn and Cr reacted with O. Therefore, oxide was formed on the surface of the flakes and on the surface of the broken HEA powder,

leading to oxide distribution predominantly inside the " slurry " layer. Since Cr reacts readily with C, Cr reacts not only with O, but also with C to produce a carbide phase.

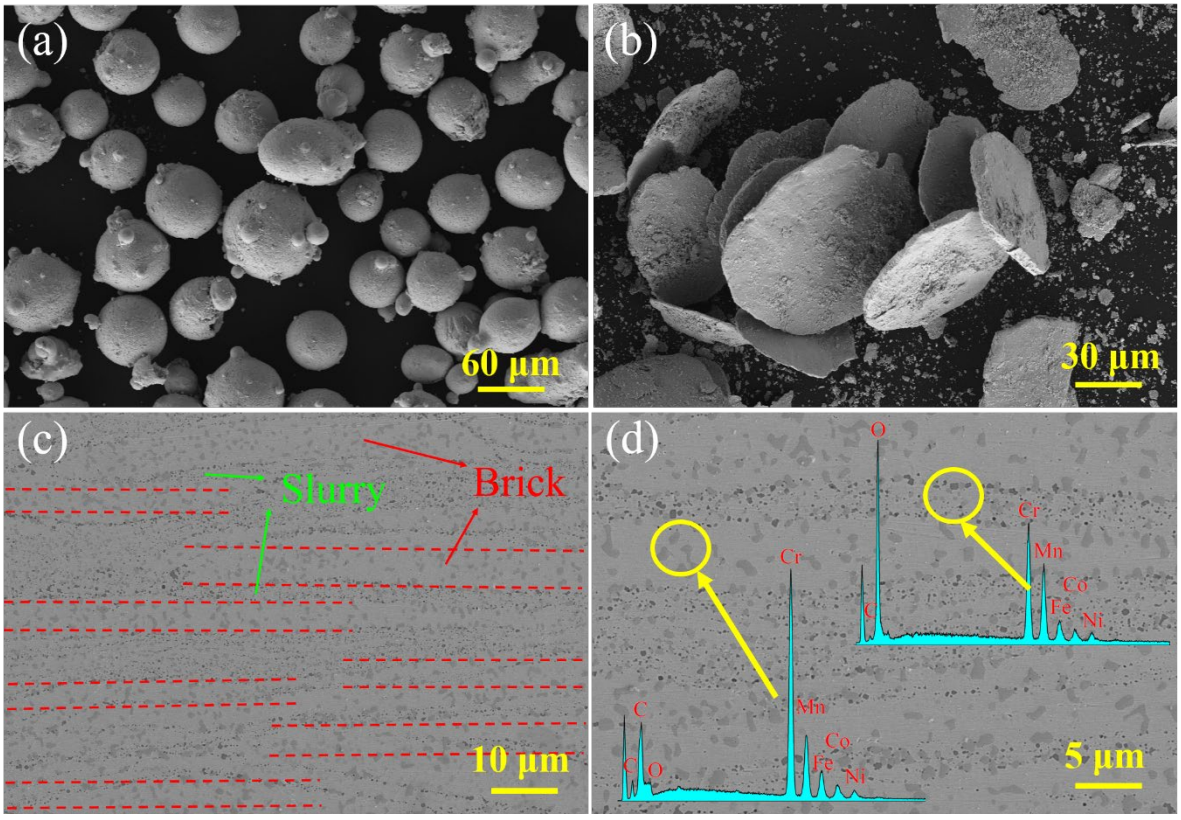


Figure 3. SEM images of powder and bulk sections: (a) raw powder, (b) flaky powder, (c, d) microstructure at low and high magnification, respectively.

To further characterize the distribution of the elements in the microstructure, the GNPs/CoCrFeNiMn HEA matrix composite cross-sections were scanned by energy spectroscopy. The SEM results in Figure 3 are further validated by the homogeneous distribution of carbon elements and the enrichment of O with Cr and Mn elements in localized areas, as shown in Figure 4. The uniform distribution of the carbide phase is due to the increased diffusion of atoms at high temperatures and pressures, resulting in C atoms entering the "brick". The oxide phase is mainly distributed in the "slurry" zone, due to the fact that Cr and Mn are easily combined with O and oxidation occurs on the surface of flaky and broken particles, therefore mainly in the "slurry" zone.

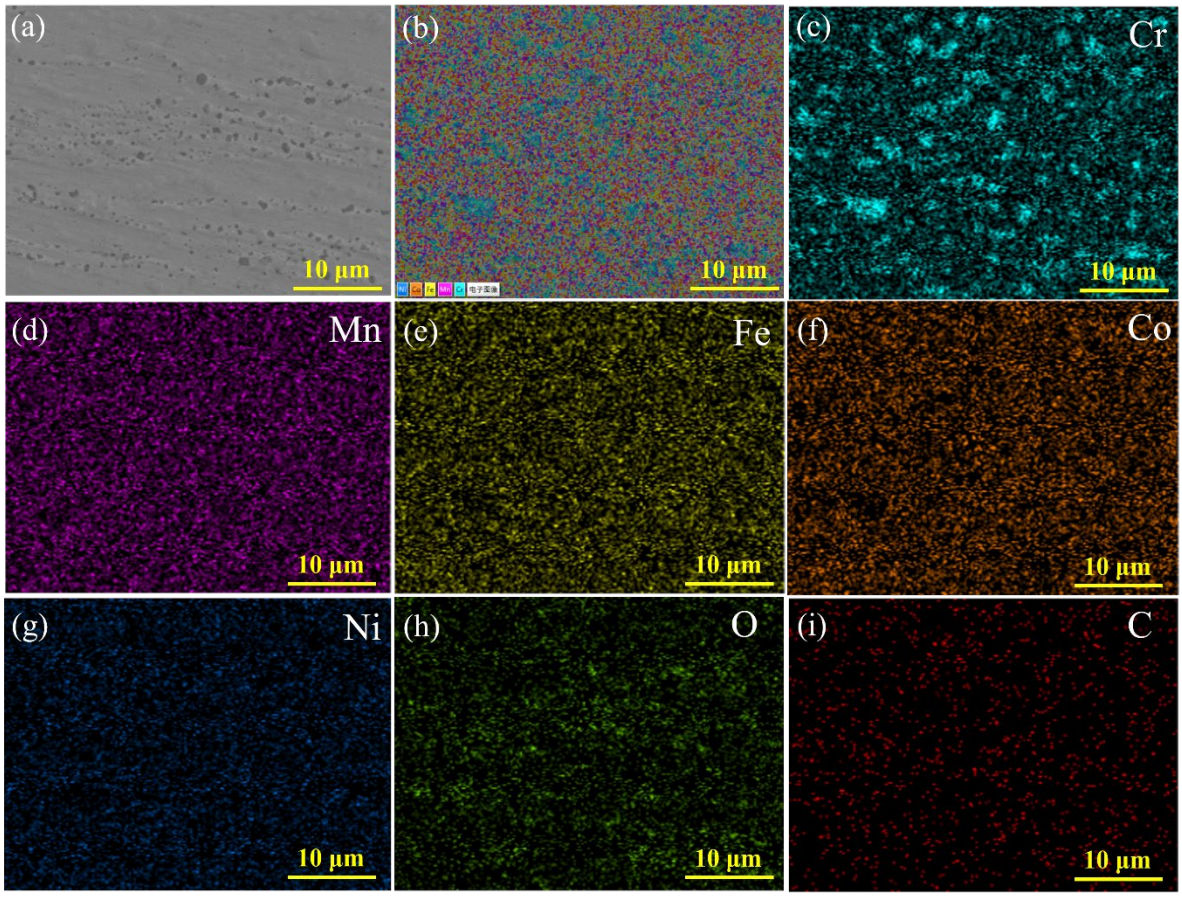


Figure 4. Elemental distribution of laminated GNPs/CoCrFeNiMn HEA matrix composites.

Figure 5 shows TEM images of the laminated GNPs/CoCrFeNiMn HEA matrix composites, further characterizing the microstructure and second phase of the composites. As shown in Figure 5(a), there are plenty of dislocations and twins in the microstructure, and the presence of dislocations and twins can ensure better mechanical properties of the composite. Due to the diversity of elements in HEA, thermal mismatch stresses are generated at grain boundaries at high temperatures, so that dislocations undergo massive plugging at grain boundaries. Figure 5(b) shows the HRTEM image of the carbide phase and the substrate, which shows that the carbide phase is well bonded to the substrate. The Fourier Transformation (FFT) shows that the crystal plane spacing between the FCC matrix and the carbide phase is 0.210nm and 0.622nm respectively, thus concluding that the carbide phase is an $M_{23}C_6$ type carbide. Selected area electron diffraction (SAED) was performed on the twins and the three phases in the microstructure, respectively. Figure 5(c) shows the diffraction pattern of the twins, which further confirms the presence of twins. Figure (d-f) show the FCC matrix, oxide phase and

carbide phase, respectively. The oxide phase is further identified as $CrMn_{1.5}O_4$ and the carbide phase as $Cr_{23}C_6$, which is confirmed with each other by the EDS results in Figure 3(d). In summary, the microstructure of the laminated GNPs/HEA matrix composites is mainly composed of $Cr_{23}C_6$, $CrMn_{1.5}O_4$ diffuse phases, FCC structured solid solution matrix phases and the presence of numerous dislocations and twins.

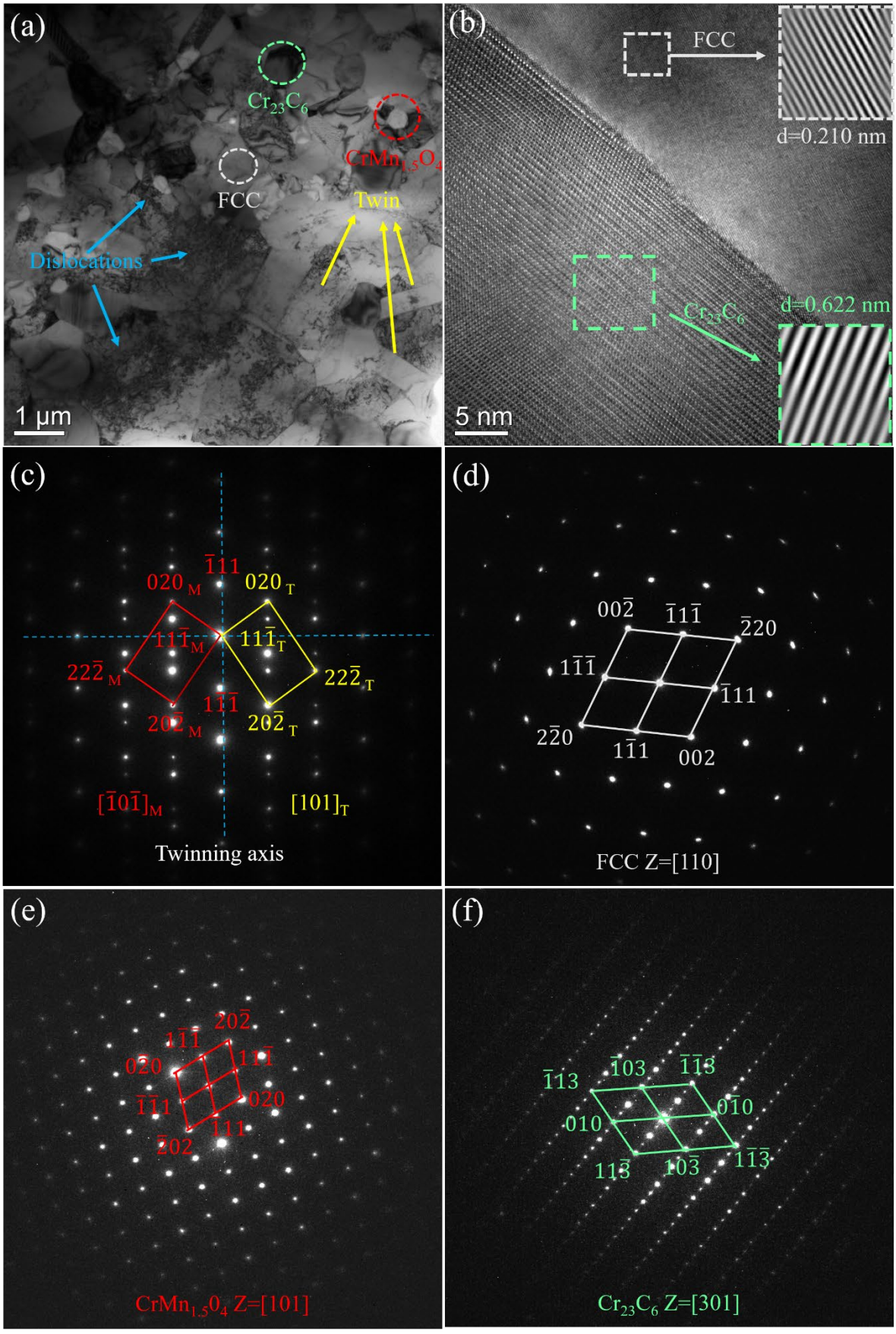


Figure 5. TEM images of the laminated GNPs/CoCrFeNiMn HEA matrix composites: (a)

TEM image of the composite; (b) HRTEM image of the carbide and matrix; (c-f) diffraction patterns of the twin, matrix, oxide and carbide phases, respectively.

3.2 Oxidation kinetics

Figure 6(a) shows the oxidation kinetic curves of the laminated GNPs/CoCrFeNiMn HEA matrix composites. In order to visualize the kinetics of the oxidation of the composite at different times, the logarithmic relationship between oxidation weight gain and oxidation time is plotted in Figure 6(b). The weight gain per unit area of the metal (alloy) during oxidation as a function of oxidation time is as follows [35, 42]:

$$\Delta W^n = k_p t \quad (1)$$

Where $\Delta W$ indicates weight gain per unit area ($mg/cm^2$), n is the power index, $k_p$ is the oxidation reaction rate constant ($mg^n/cm^{2n}$) and t is the oxidation time (h). In addition, temperature, oxygen partial pressure, the state of the substrate surface and the properties of the oxide film all influence the kinetics of the oxidation of the metal (alloy).

Common oxidation kinetic curves are linear, parabolic and cubic curves [43]. Generally, at the same temperature, a higher $k_p$ value for the same type of curve indicates a poorer oxidation resistance of the alloy. The increase in mass of the alloy is due to a gradual increase in mass as the O element diffuses, the oxide increases and the thickness of the oxide scales increases. After 100 h of long-term oxidation, the composites showed mass gains of approximately 0.48, 0.75, 1.16, 1.34, 1.48, 1.55, 1.63 and 1.75 $mg/cm^2$ at 12 h intervals respectively. As can be seen in Figure 6(a), a significant oxidation weight gain occurred in the HEA composite. The results of the curve fitting in the table show that during the pre-oxidation period of 0-48 h, the oxidation reaction level $n \approx 1.3$, which approximates a linear rate oxidation law, indicating that the oxidation process occurring during the pre-oxidation period is very violent. In contrast, during the long-term oxidation process of 48-100 h, the oxidation reaction level $n \approx 2.9$, which approximates the exponential rate oxidation law, indicating that the HEA matrix composite forms an oxide film with some protection as oxidation occurs. G. Laplanche et al. [36] also worked on the oxidation behavior of CrMnFeCoNi at 600-900 ℃ for 100 h. The results also

showed an initial linear oxidation rate which became parabolic after a longer time.

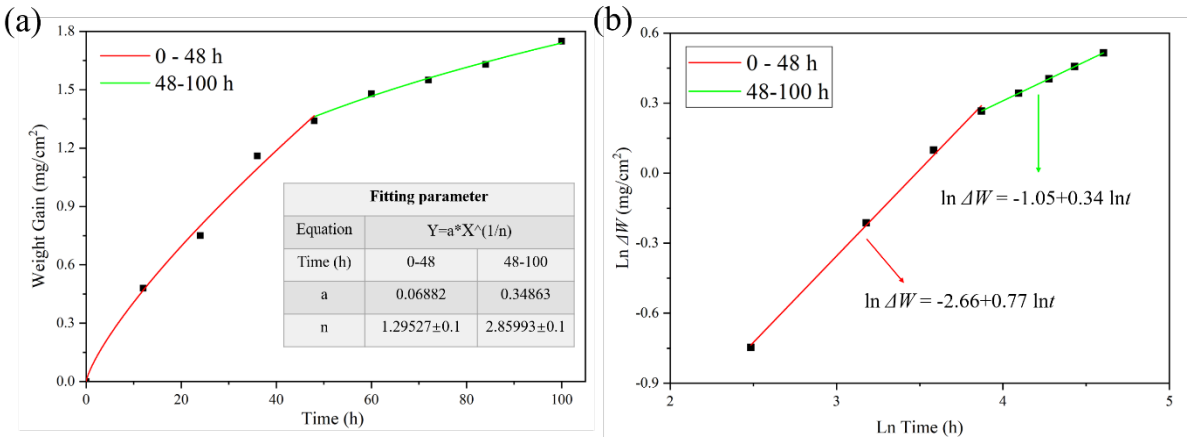


Figure 6. Laminated GNPs/CoCrFeNiMn HEA matrix composites: (a) oxidation kinetic curves; (b) oxidation kinetic characteristic curves.

3.3 Surface Morphology and Phases

Figure 7 shows the XRD spectrum of the laminated GNPs/CoCrFeNiMn HEA matrix composites after 24-100h of water steam oxidation at 1000 °C. Mn and Cr are highly susceptible to oxidation, forming Mn-rich and Cr-rich oxide scales. As the oxidation time increases, the content of $(Mn, Cr)_3O_4$ gradually increases, while the relative content of $Mn_2O_3$ decreases. W. Kai et al. [33] found that the iso-atomic ratio CoCrFeNiMn HEA consists of an outer single-phase $Mn_3O_4$ layer, an intermediate $(Cr, Mn)_3O_4$ layer and an inner $Cr_2O_3$ layer, regardless of the selected oxygen partial pressure. N.K. Adomako et al. [44] experimentally concluded that the addition of Mn enhanced the oxidation kinetics, while Cr reduced the kinetics. G. Laplanche et al. [36] concluded that the growth of Mn-oxide is the rate step controlling the oxidation kinetics of CoCrFeNiMn and that the outward diffusion of Mn ions would control the oxidation kinetics. Oxidation of CoCrFeNiMn produces mainly oxides of Mn and Cr, rather than Fe, Co and Ni, as the former has a more negative Gibbs free energy than the latter. The intense firing of Mn and Cr with O leads to the rapid formation of oxide scales and the formation of an elemental depletion zone in the region below the oxide scales, resulting in its increased oxidation resistance.

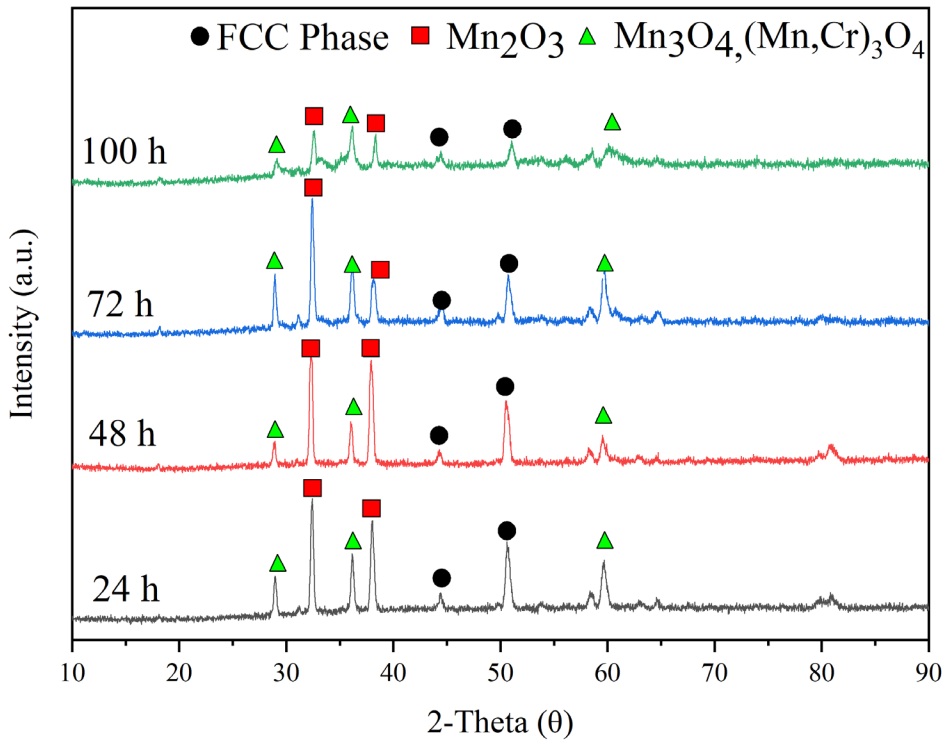


Figure 7. XRD image of the laminated GNPs/CoCrFeNiMn HEA matrix composite with water steam oxidation at 1000 ℃.

Scanning electron microscopy (SEM) and energy spectroscopy (EDS) were used to observe the oxidation morphology after short and long term high-temperature water steam oxidation (as shown in Figure 8. As shown in Figure 8(a-b), during the early oxidation process of 24h, an oxide film was formed on the surface of the composite. The oxide film surface was sparse and porous, which provided a channel for oxygen to enter and accelerated the formation of the oxide scales. In addition, there are some oxide clusters on the surface of the composite, which are known to be Mn-rich oxides by EDS analysis. Figure 8(c-d) shows the surface morphology of the 100h long-term oxidation, the surface has become dense and lost the early sparse porous structure, which is good for the oxidation resistance of the substrate. However, some exfoliation has begun to occur on the surface of the composite, and EDS analysis shows that the exfoliated component is an Mn-rich oxide. It is similar to the XRD results that the Mn in the CoCrFeNiMn HEA composite reacts very easily with O. The oxide scales on the surface consists mainly of Mn-oxide. As a result, it can be seen that the laminated GNPs/CoCrFeNiMn

HEA matrix composites rapidly form a thin oxide scales in the early stages and gradually dense with oxidation time, thus enhancing their oxidation resistance. F. Ye et al. [45] also experimentally found that the grain boundary effect and the Cr and Mn interface were more conducive to the outward diffusion of Mn elements and the formation of tight oxide films.

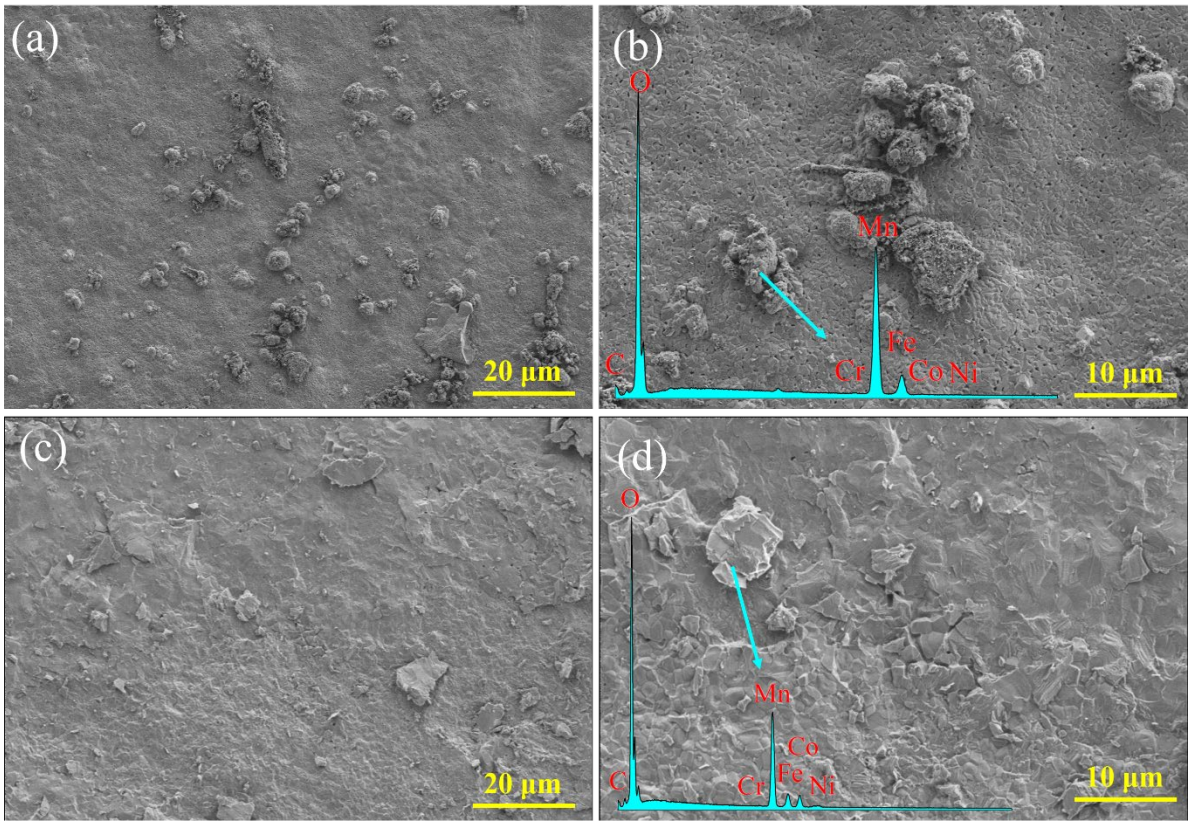


Figure 8. Surface oxidation morphology of laminated GNPs/CoCrFeNiMn HEA matrix composites: (a, b) 24h; (c, d) 100h.

W. Kai et al. [33] also detected quantities of $Mn_3O_4$, $(Mn, Cr)_3O_4$ and $Cr_2O_3$ in both the outer and middle layers of the oxide. They found that the cause could be the rapid reaction of MnO with oxygen to form $Mn_3O_4$ with a high oxygen content. secondly, the formation of ternary $(Mn, Cr)_3O_4$ oxides under the action of a suitable solid solution between MnO and $Cr_2O_3$. That is why the oxide scales forms rapidly and is thin and porous. In the multiphase effect [46], the formation of $Cr_2O_3$, $(Mn, Cr)_3O_4$ and $Mn_3O_4$ triple complexes on the intermediate scale with complete consumption of MnO is kinetically beneficial. And in $Cr_2O_3$ sub-lattices, the order of diffusion coefficients is $Mn^{+2} > Fe^{+2} > Ni^{+2} > Cr^{+3}$, with Mn cations diffusing much faster than Cr ions [47]. Therefore, the outward diffusion of Mn ions is much faster than the diffusion of other cations, which in turn forms a porous Mn-containing oxide scales on the $Cr_2O_3$ layer.

### 3.4 Cross-section Observation of Oxide Scale

To further analyze the high-temperature water steam oxidation of the laminated HEA matrix composites in the early and later stages, the cross-sectional oxide scales were observed using SEM, as shown in Figure 9. Figure 9(a, c) shows the oxidation cross-sections in the vertical laminated direction at 24 h and 100 h, respectively. An oxide scales with a thickness of 19.56 μm was formed in the first part of the 24 h period, which then increased to 31.45 μm until 100 h. In both Figure 9(a) and (c), internal oxides are observed, diffusing locally to the interior below the oxide scales, so it can be assumed that the composite is more effective in resisting high-temperature water steam. Figure 9(b, d) shows oxidation cross sections in the parallel laminated direction at 24 h and 100 h, respectively, with oxide scales thicknesses of 23.77 and 34.56 μm. In the parallel laminated direction, the internal oxides all diffuse along the interlayer. Substantial amounts of internal oxide are produced below the oxide scales, with a tendency to diffuse downwards, as shown in Figure 9(b). In contrast, after the prolonged oxidation in Figure 9(d), oxygen diffuses through the "slurry" layers into the interior, generating a large number of oxides distributed between the "brick" layers. As a result, SEM images after prolonged oxidation show that the oxide layer tends to expand along the "slurry" layer of the laminate structure towards the interior of the composite.

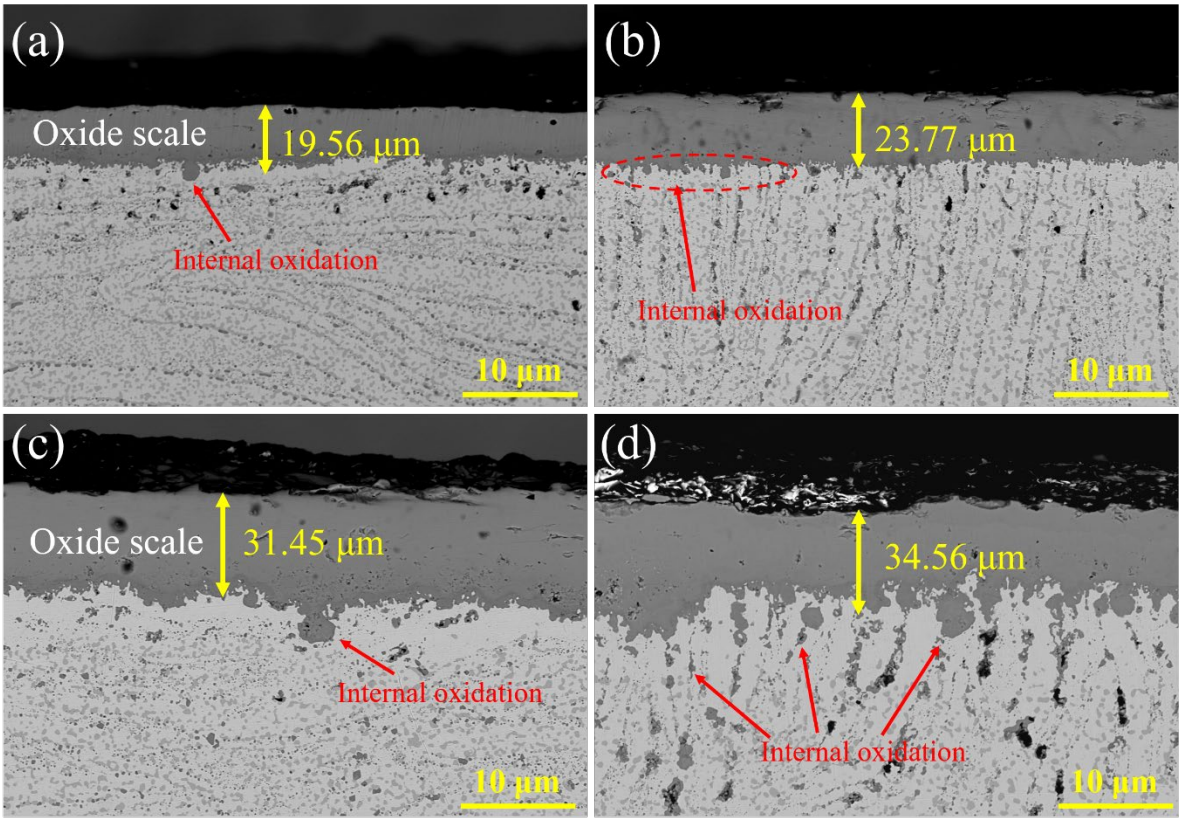


Fig. 9 SEM images of the cross-sectional oxide scales of the laminated GNPs/CoCrFeNiMn HEA matrix composite: (a, b) 24 h; (c, d) 100 h

The cross-sectional elemental distribution was further analyzed by energy spectrometry (EDS) to give a clearer picture of the distribution of the elements during the oxidation process, as shown in Figure 10. During the 24 h pre-oxidation process, a homogeneous and relatively dense oxide scales has been formed, which is Mn-rich externally and Cr-rich internally. The low elemental content of Mn beneath the oxide scales suggests that the large diffusion of Mn into the outer layers during oxidation reacts with O, resulting in a reduction of the inner elemental content. And in the later oxidation period of 100 h (as in Figure 10b), it was found that the oxide scales only thickened, indicating that the oxide scales was spreading evenly inwards. Meanwhile, the obvious depletion zone of elements (Mn and Cr) appears below the oxide scales, which is very beneficial to the oxidation resistance of the composite. The depletion of the elements (Mn and Cr) is reduced, and the remaining elements are less likely to react with O. This makes it difficult for O to enter the composite, which effectively enhances the oxidation resistance. A. Ferrari et al. [48] calculated the free energy of formation of various metal oxides and found that the binding of O promoted strong deviations of Cr and Mn of all

compositions. K.Y. Tsai et al. [49] reported the typical slow diffusion behavior of the CoCrFeNiMn alloy and found that the elemental diffusion coefficients Mn > Cr > Fe > Co > Ni. D. Gaertner et al. [50] also measured the self-diffusion of Co, Cr, Fe and Ni in iso-atomic HEA single crystals, as well as the solute diffusion of Mn in CoCrFeNi, and showed that Mn diffuses fastest in the tetrad and pentad alloys. In the cross-sectional SEM image of Fig. 3 and the elemental distribution image of Fig. 4, the element C is uniformly distributed in the microstructure of the composite in the form of carbide. However, there are several unique C element distribution points in Fig. 10, which are the result of the impurities present on the surface of the sample during the photographing process, causing the element distribution to appear different.

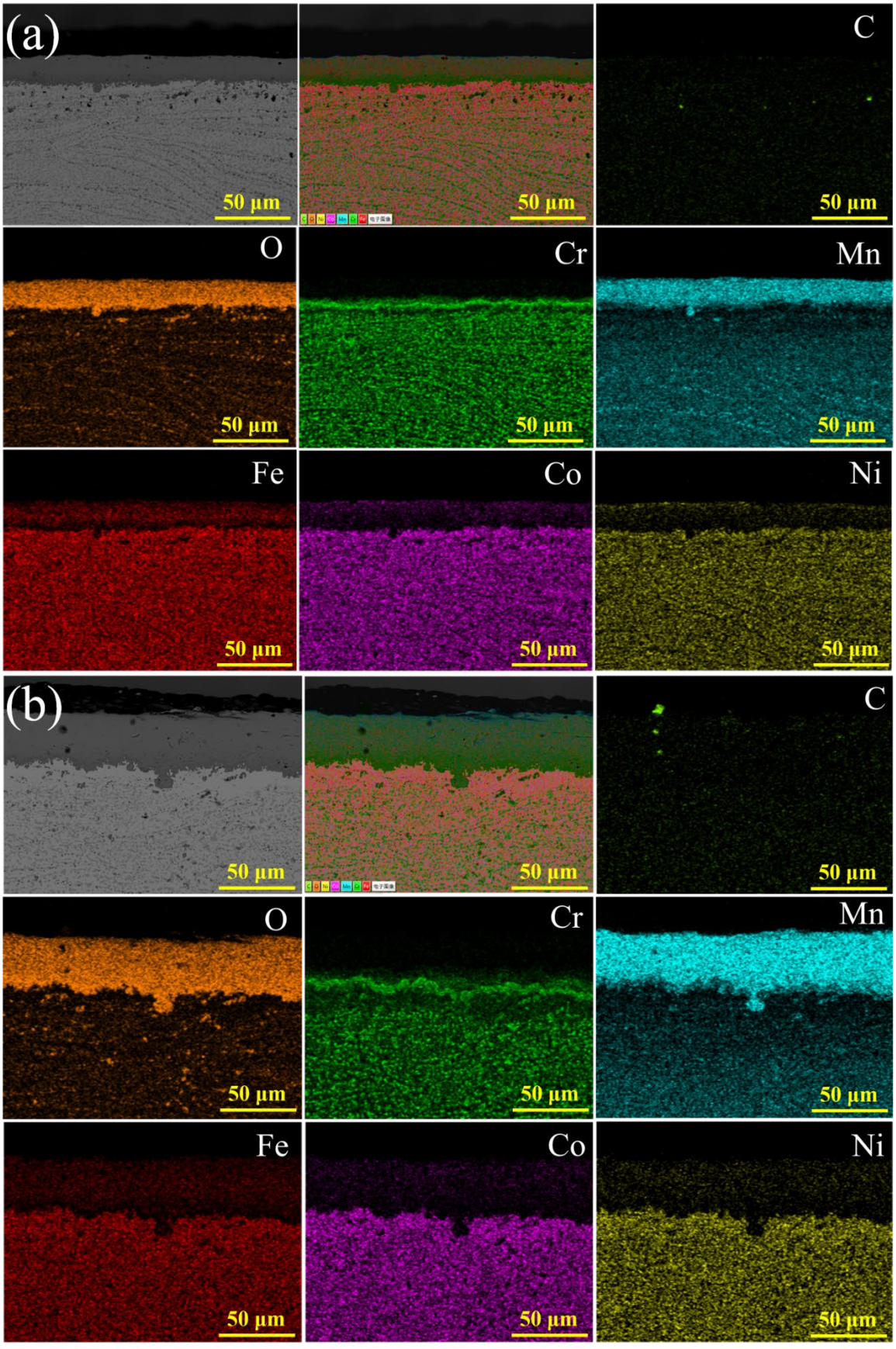


Figure 10. Image of the elemental distribution of the oxide cross-section of the laminated

GNPs/CoCrFeNiMn HEA matrix composite.

Figure 11 shows the results of further SEM and EDS analysis of the composite. The results show that the thickness of the oxide scales increases significantly after 100h compared to the oxidation cross section of 12h. The composition of the oxide scales didn't change significantly after the composite was oxidized in a water steam environment for long periods of time. The oxide scales is inferred by EDS to be Mn and Cr, with the outer layer rich in Mn and memory rich in Cr (as in Figure 11c), and the Cr layer thickens in the oxide scales after 100 h (as in Figure 11f). Thus, during the high-temperature water steam oxidation of the laminated GNPs/CoCrFeNiMn HEA matrix composites, Mn is most likely to react in contact with O and generate an external Mn-rich oxide scales. As the Mn element diffuses outwards, it leads to a reduction in the Mn content of the inner layer. At the same time, the O element diffuses inwards, reaching the inner oxide scales and depleting the Mn element. Among Co, Cr, Fe and Ni, the Cr is more easily bound by O. Therefore, a further Cr-rich oxide scales is formed within the external Mn-rich oxide scales. The depleted zones of Mn and Cr elements formed inside the oxide scales effectively prevent the diffusion of O atoms into the interior of the matrix. In the work of other workers, it has also been found that for CoCrFeNiMn HEA, prolonged exposure to air results in the formation of an external $Mn_2O_3$ layer and an internal $Cr_2O_3$ layer [32, 51]. N.K. Adomako et al. [44] similarly noted $Cr_2O_3$ layers at the matrix/oxide interface and detected depleted zones of Mn and Cr below such oxide scales. J.Y. He et al. [52] also revealed that the typical structure of CoCrFeNiMn HEA is an inner layer of Cr oxide ($Cr_2O_3$), with the outer layer tending towards Mn oxide. Four stable oxides exist in the Mn-O system, namely MnO, $Mn_3O_4$, $Mn_2O_3$ and $MnO_2$, while $Cr_2O_3$ is the only stable crystalline phase in the Cr-O system [53].

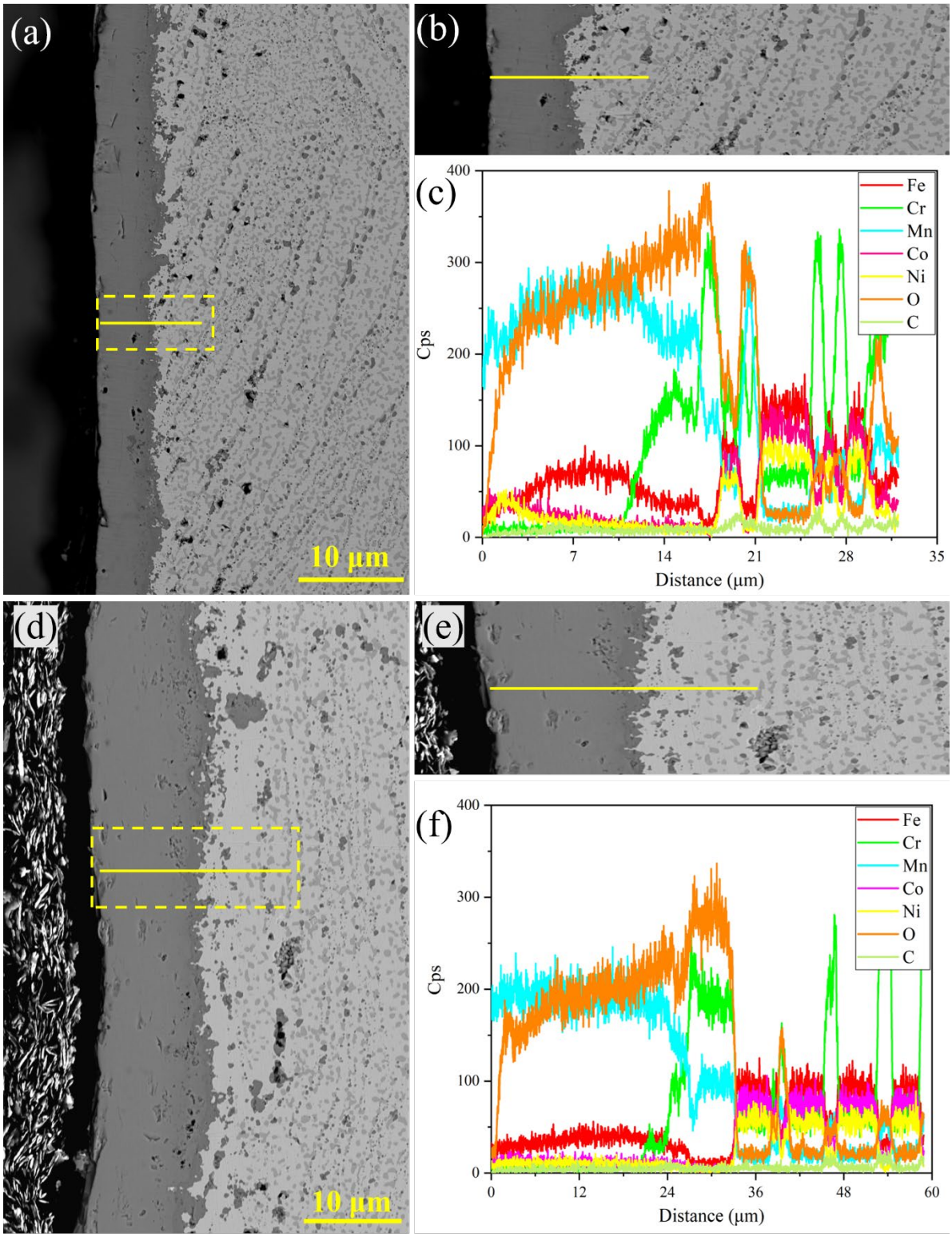


Fig. 11. SEM-EDS line analysis of water steam oxidation cross-sections of laminated GNPs/CoCrFeNiMn HEA matrix composites at 1000 ℃: (a-c) 12 h, (d-f) 100 h.

3.5 Oxidation Mechanism Analysis

The high-temperature oxidation of alloys is a very complex process which involves not only physical but also chemical reactions [54]. When oxygen molecules contact the alloy, oxygen molecules are physically adsorbed onto the alloy surface due to the presence of intermolecular forces. Subsequently, the oxygen molecule breaks down into oxygen atoms and interacts with the metal atoms to produce a metal oxide which grows laterally as an oxide film. The oxide generated on the outside of the alloy separates the substrate from the oxygen. The diffusion of oxygen and metal ions is hindered, but they are not completely isolated. Material transport can still occur through the oxide film and therefore the oxide film will continue to grow thicker as the oxidation process progresses. The laminated structure gives the material different morphological characteristics in different directions, which also leads to different properties, resulting in anisotropy of structure and properties [18, 55-57]. The oxidation mechanism of the laminated GNPs/CoCrFeNiMn HEA matrix composites in water steam oxidation at 1000 ℃ was investigated based on the SEM images of the oxidation cross-sections in Figure 9 and Figure 10, as shown in Figure 12. The formation of the laminate structure can be clearly observed in Figure 3, where the interlayer graphene is attached to the HEA substrate, forming alternating layers of HEA and graphene, forming an interlayer interlocking pattern of the nacreous shell structure [58]. The key advantage of nano-carbon reinforced laminated composites is that it ensures the parallel alignment of the carbon nanosheets in the tensile direction. It also forms a strong interface with the metal matrix, enabling the nano-carbon to fully exploit its load-bearing capacity and to a certain extent impede the diffusion of oxygen atoms. Therefore, the laminate structure is able to exert excellent antioxidant properties during the corrosion process of high-temperature oxidation by virtue of its unique microstructure.

As shown in Figure 12(a), during the oxidation of high-temperature water steam, oxygen ions diffuse inwards and metal cations ($Mn^{2+}$ and $Cr^{3+}$) diffuse outwards. Y.-K. Kim et al. [37] similarly found that the high-temperature oxidation behavior of CoCrFeNiMn HEAs was mainly influenced by the Cr and Mn elements. The easier combination of Mn and O leads to the rapid formation of Mn-rich oxides in the outermost layers, which rapidly expand into oxide scales. With the reduction of Mn ions and further diffusion of O ions, $Cr^{3+}$ combines with O

below the Mn-rich oxide scales to form an internal Cr-rich oxide scales. As oxidation proceeds, the internal Mn and Cr elements diffuse to the surface to form an oxide scales, resulting in the formation of a certain area of elemental depletion of Mn and Cr beneath the oxide scales. Thus, the oxide scales appears as an external Mn-rich layer, an internal Cr-rich layer and an elemental depletion layer in the matrix close to the oxide scales. The presence of the elemental depletion zone prevents further diffusion of O ions to the interior and therefore further oxidation corrosion. The cation diffusion coefficients of alloying elements in oxides are essential for understanding the development of oxide scales. R.E. Lobnig et al. [47] found that the diffusion coefficients of the four cations $Mn^{2+}$, $Fe^{2+}$, $Ni^{2+}$ and $Cr^{2+}$ through $Cr_2O_3$ ranged from fast to slow. Kautz E J et al. [59] discovered that Cr-rich oxides form first on HEAs, while Mn and Fe cations have higher diffusivity and are therefore more likely to form oxide in the outer layers.

As shown in Figure 12(b), due to the anisotropy of the laminated structure, the oxidation mechanism is also different in the parallel laminated direction versus the perpendicular laminated direction. In the vertical lamellar direction, the oxide scales are evenly distributed and grow parallel to each other, as a result of the unique " brick-slurry " structure of the laminate. When the oxygen ions enter the composite matrix in the vertical laminated direction, they are affected by the laminated structure and do not easily break through the GNPs layer between the layers. The result is a homogeneous parallel oxide scales structure, demonstrating the better antioxidant properties of the laminated HEA. However, in the parallel laminated direction, the O ions can expand inwards along the "slurry" layer, forming a large amount of internal oxide and causing more oxidation corrosion damage to the substrate. As a result, the laminated GNPs/CoCrFeNiMn HEA matrix composites exhibit strong oxidation resistance in the vertical laminated direction.

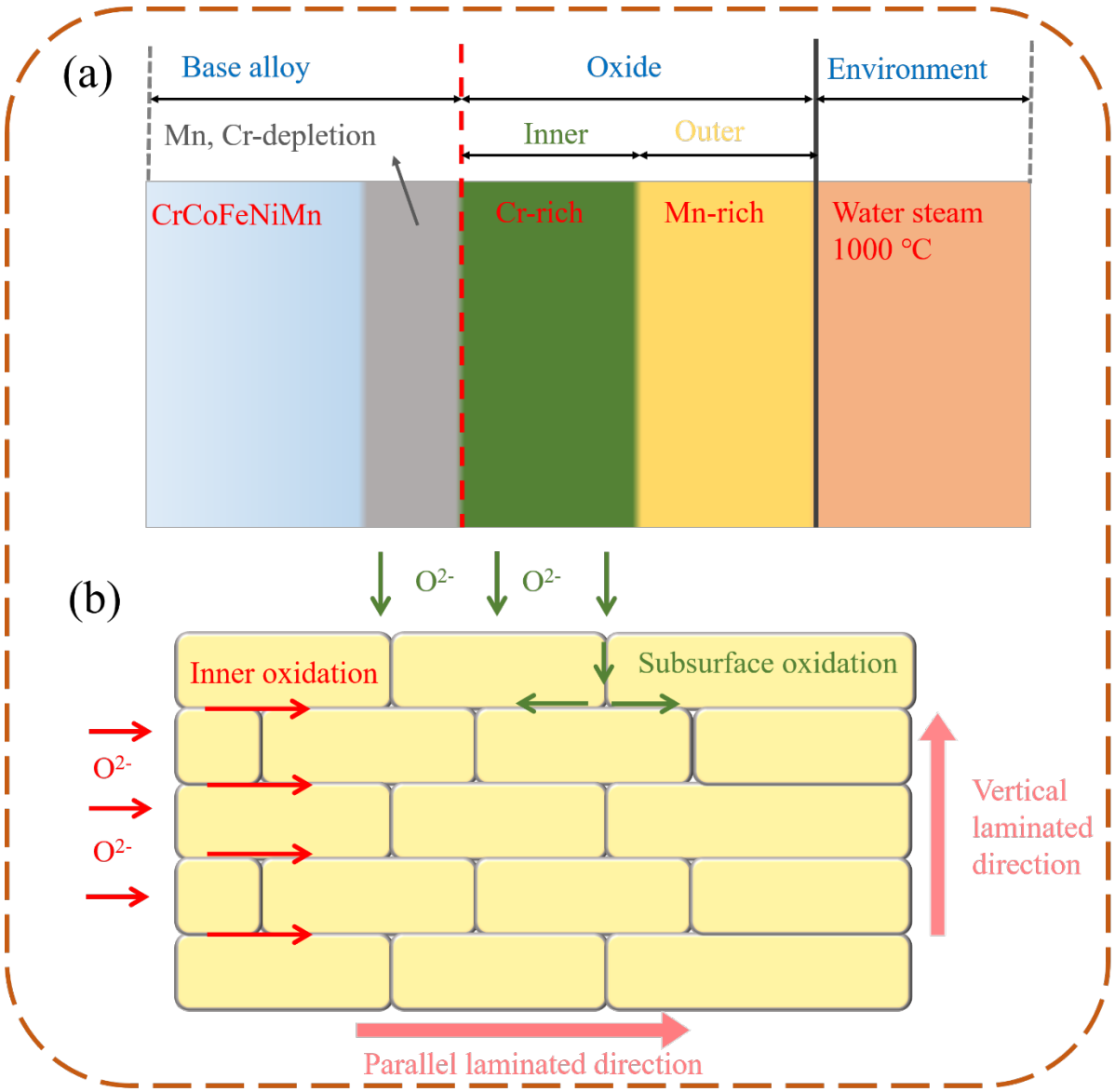


Figure 12. Schematic diagram of the water steam oxidation mechanism of the laminated GNPs/CoCrFeNiMn HEA matrix composite at 1000 °C.

## 4 Conclusion

The GNPs/CoCrFeNiMn HEA matrix composites with laminated structure were successfully prepared by mechanical ball milling and powder metallurgy. The isothermal oxidation behavior at 1000 °C was also studied and the following conclusions were obtained:

(1) Laminated structures can be successfully prepared by mechanical ball milling and powder metallurgy. The composites maintain a single FCC matrix phase, with massive dislocations and twinning within the grains, while the presence of $CrMn_{1.5}O_4$ and $Cr_{23}C_6$ diffuse phases also

leads to secondary phase strengthening.

(2) The composites oxidize faster in the short term and slower in the long term. The elemental diffusion of Mn and Cr controls the entire oxidation process, with Mn and Cr forming oxide films rapidly in the early stages. As the oxidation proceeds, the diffusion of Mn and Cr slows down and the growth of the oxide scales gradually stabilizes.

(3) The results of the XRD analysis after the high-temperature water steam oxidation test show that the matrix is FCC phase and the oxide scales is mainly $Mn_2O_3$ and $(Mn, Cr)_3O_4$. The external oxide scales is mainly $(Mn, Cr)_3O_4$ and the internal layer is $Cr_2O_3$. Furthermore, there are elemental depletion zones for Mn and Cr.

(4) The laminated structure controls the diffusion path of oxygen ions and changes the direction of diffusion of oxygen ions to the interior along the "slurry" layer. Thus, there is excellent oxidation resistance in the vertical laminated direction.

## Conflict of interest

The authors declare that they have no conflict of interest.


## Acknowledgements

This work was supported by Key Laboratory of Infrared Imaging Materials and Detectors, Shanghai Institute of Technical Physics, Chinese Academy of Sciences (No. IIMDKFJJ-21-10) and China Postdoctoral Science Foundation (No. 2018T110993). We would like to thank Analytical and Testing Center of Southwest Jiaotong University for partial testing.


## Data Availability statement

The data used to support the findings of this study are available from the corresponding author upon request.

## References


[1] J.C. Williams, E.A. Starke, Progress in structural materials for aerospace systems, Acta

Mater. 51(19) (2003) 5775-5799. https://doi.org/10.1016/j.actamat.2003.08.023.

[2] M. Schütze, W.J. Quadakkers, Future directions in the field of high-temperature corrosion research, Oxid Met. 87(5-6) (2017) 681-704. https://doi.org/10.1007/s11085-017-9719-3.

[3] J.W. Yeh, Alloy design strategies and future trends in high-entropy alloys, Jom-Us. 65(12) (2013) 1759-1771. https://doi.org/10.1007/s11837-013-0761-6.

[4] J.M. Zhu, H.M. Fu, H.F. Zhang, A.M. Wang, H. Li, Z.Q. Hu, Synthesis and properties of multiprincipal component AlCoCrFeNiSi$_x$ alloys, Mat Sci Eng A-Struct. 527(27-28) (2010) 7210-7214. https://doi.org/10.1016/j.msea.2010.07.049.

[5] Y.L. Chou, Y.C. Wang, J.W. Yeh, H.C. Shih, Pitting corrosion of the high-entropy alloy Co$_{1.5}$CrFeNi$_{1.5}$Ti$_{0.5}$Mo$_{0.1}$ in chloride-containing sulphate solutions, Corros Sci. 52(10) (2010) 3481-3491. https://doi.org/10.1016/j.corsci.2010.06.025.

[6] B. Gludovatz, A. Hohenwarter, D. Catoor, E.H. Chang, E.P. George, R.O. Ritchie, A fracture-resistant high-entropy alloy for cryogenic applications, Science. 345(6201) (2014) 1153-8. https://doi.org/10.1126/science.1254581.

[7] B. Cantor, I.T.H. Chang, P. Knight, A.J.B. Vincent, Microstructural development in equiatomic multicomponent alloys, Mat Sci Eng A-Struct. 375-377 (2004) 213-218. https://doi.org/10.1016/j.msea.2003.10.257.

[8] F. Otto, A. Dlouhý, C. Somsen, H. Bei, G. Eggeler, E.P. George, The influences of temperature and microstructure on the tensile properties of a CoCrFeMnNi high-entropy alloy, Acta Mater. 61(15) (2013) 5743-5755. https://doi.org/10.1016/j.actamat.2013.06.018.

[9] N. Stepanov, M. Tikhonovsky, N. Yurchenko, D. Zyabkin, M. Klimova, S. Zherebtsov, A. Efimov, G. Salishchev, Effect of cryo-deformation on structure and properties of CoCrFeNiMn high-entropy alloy, Intermetallics. 59 (2015) 8-17. https://doi.org/10.1016/j.intermet.2014.12.004.

[10] Z. Wu, H. Bei, G.M. Pharr, E.P. George, Temperature dependence of the mechanical properties of equiatomic solid solution alloys with face-centered cubic crystal structures, Acta Mater. 81 (2014) 428-441. https://doi.org/10.1016/j.actamat.2014.08.026.

[11] F. Otto, N.L. Hanold, E.P. George, Microstructural evolution after thermomechanical

processing in an equiatomic, single-phase CoCrFeMnNi high-entropy alloy with special focus on twin boundaries, Intermetallics. 54 (2014) 39-48. https://doi.org/10.1016/j.intermet.2014.05.014.

[12] W.Y. Chen, M.A. Kirk, N. Hashimoto, J.W. Yeh, X. Liu, Y. Chen, Irradiation effects on $Al_{0.3}$CoCrFeNi and CoCrMnFeNi high-entropy alloys, and 316H stainless steel at 500 ℃, J Nucl Mater. 539 (2020). https://doi.org/10.1016/j.jnucmat.2020.152324.

[13] J. Chen, X. Zhou, W. Wang, B. Liu, Y. Lv, W. Yang, D. Xu, Y. Liu, A review on fundamental of high entropy alloys with promising high-temperature properties, J Alloy Compd. 760 (2018) 15-30. https://doi.org/10.1016/j.jallcom.2018.05.067.

[14] J.Y. He, H. Wang, H.L. Huang, X.D. Xu, M.W. Chen, Y. Wu, X.J. Liu, T.G. Nieh, K. An, Z.P. Lu, A precipitation-hardened high-entropy alloy with outstanding tensile properties, Acta Mater. 102 (2016) 187-196. https://doi.org/10.1016/j.actamat.2015.08.076.

[15] T. Borkar, B. Gwalani, D. Choudhuri, C.V. Mikler, C.J. Yannetta, X. Chen, R.V. Ramanujan, M.J. Styles, M.A. Gibson, R. Banerjee, A combinatorial assessment of $Al_x$CrCuFeNi$_2$ ($0 < x < 1.5$) complex concentrated alloys: Microstructure, microhardness, and magnetic properties, Acta Mater. 116 (2016) 63-76. https://doi.org/10.1016/j.actamat.2016.06.025.

[16] W. Huang, D. Restrepo, J.Y. Jung, F.Y. Su, Z. Liu, R.O. Ritchie, J. McKittrick, P. Zavattieri, D. Kisailus, Multiscale toughening mechanisms in biological materials and bioinspired designs, Adv Mater. 31(43) (2019) e1901561. https://doi.org/10.1002/adma.201901561.

[17] U.G.K. Wegst, M.F. Ashby, The mechanical efficiency of natural materials, Philos Mag. 84(21) (2004) 2167-2186. https://doi.org/10.1080/14786430410001680935.

[18] L. Meng, X. Wang, J. Ning, X. Hu, G. Fan, K. Wu, Beyond the dimensional limitation in bio-inspired composite: Insertion of carbon nanotubes induced laminated Cu composite and the simultaneously enhanced strength and toughness, Carbon. 130 (2018) 222-232. https://doi.org/10.1016/j.carbon.2018.01.006.

[19] Z. Yu, W. Yang, C. Zhou, N. Zhang, Z. Chao, H. liu, Y. Cao, Y. Sun, P. Shao, G. Wu, Effect of ball milling time on graphene nanosheets reinforced Al6063 composite fabricated by

pressure infiltration method, Carbon. 141 (2019) 25-39. https://doi.org/10.1016/j.carbon.2018.09.041.

[20] X.N. Mu, H.N. Cai, H.M. Zhang, Q.B. Fan, F.C. Wang, Z.H. Zhang, Y. Wu, Y.X. Ge, S. Chang, R. Shi, Y. Zhou, D.D. Wang, Uniform dispersion of multi-layer graphene reinforced pure titanium matrix composites via flake powder metallurgy, Mat Sci Eng A-Struct. 725 (2018) 541-548. https://doi.org/10.1016/j.msea.2018.04.056.

[21] S.R. Bakshi, D. Lahiri, A. Agarwal, Carbon nanotube reinforced metal matrix composites - a review, Int Mater Rev. 55(1) (2013) 41-64. https://doi.org/10.1179/095066009x12572530170543.

[22] S. Guan, D. Wan, K. Solberg, F. Berto, T. Welo, T.M. Yue, K.C. Chan, Additively manufactured CrMnFeCoNi/AlCoCrFeNi$Ti_{0.5}$ laminated high-entropy alloy with enhanced strength-plasticity synergy, Scripta Mater. 183 (2020) 133-138. https://doi.org/10.1016/j.scriptamat.2020.03.032.

[23] Y. Yang, J. Hu, X.Y. Liu, W. Xu, B. Li, G.P. Ling, X.Y. Pang, Y.Z. Tian, Post treatment of an additively manufactured composite consisting of 304L stainless steel and CoCrFeMnNi high-entropy alloy, Mat Sci Eng A-Struct. 831 (2022). https://doi.org/10.1016/j.msea.2021.142104.

[24] C. Shu, Z. Yao, W. Du, X. Tao, S. Zhang, Microstructure and mechanical properties of TiC/multi-principal-component alloy composites with biomimetic micro-laminated structure, Vacuum. 206 (2022). https://doi.org/10.1016/j.vacuum.2022.111513.

[25] C. Tang, H. Shi, A. Jianu, A. Weisenburger, G. Victor, M. Grosse, G. Müller, H.J. Seifert, M. Steinbrück, High-temperature oxidation of AlCrFeNi-(Mn or Co) high-entropy alloys: Effect of atmosphere and reactive element addition, Corros Sci. 192 (2021). https://doi.org/10.1016/j.corsci.2021.109809.

[26] Y. Wang, M. Zhang, J. Jin, P. Gong, X. Wang, Oxidation behavior of CoCrFeMnNi high entropy alloy after plastic deformation, Corros Sci. 163 (2020). https://doi.org/10.1016/j.corsci.2019.108285.

[27] J. Lu, Y. Chen, H. Zhang, L. He, R. Mu, Z. Shen, X. Zhao, F. Guo, Y/Hf-doped

$Al_{0.7}$CoCrFeNi high-entropy alloy with ultra oxidation and spallation resistance at 1200 °C, Corros Sci. 174 (2020). https://doi.org/10.1016/j.corsci.2020.108803.

[28] K.F. Quiambao, S.J. McDonnell, D.K. Schreiber, A.Y. Gerard, K.M. Freedy, P. Lu, J.E. Saal, G.S. Frankel, J.R. Scully, Passivation of a corrosion resistant high entropy alloy in non-oxidizing sulfate solutions, Acta Mater. 164 (2019) 362-376. https://doi.org/10.1016/j.actamat.2018.10.026.

[29] P. Lu, J.E. Saal, G.B. Olson, T. Li, O.J. Swanson, G.S. Frankel, A.Y. Gerard, K.F. Quiambao, J.R. Scully, Computational materials design of a corrosion resistant high entropy alloy for harsh environments, Scripta Mater. 153 (2018) 19-22. https://doi.org/10.1016/j.scriptamat.2018.04.040.

[30] K.C. Lo, Y.J. Chang, H. Murakami, J.W. Yeh, A.C. Yeh, An oxidation resistant refractory high entropy alloy protected by $CrTaO_4$-based oxide, Sci Rep-Uk. 9(1) (2019) 7266. https://doi.org/10.1038/s41598-019-43819-x.

[31] O.N. Senkov, S.V. Senkova, D.M. Dimiduk, C. Woodward, D.B. Miracle, Oxidation behavior of a refractory $NbCrMo_{0.5}Ta_{0.5}TiZr$ alloy, J Mater Sci. 47(18) (2012) 6522-6534. https://doi.org/10.1007/s10853-012-6582-0.

[32] G.R. Holcomb, J. Tylczak, C. Carney, Oxidation of CoCrFeMnNi High Entropy Alloys, Jom-Us. 67(10) (2015) 2326-2339. https://doi.org/10.1007/s11837-015-1517-2.

[33] W. Kai, C.C. Li, F.P. Cheng, K.P. Chu, R.T. Huang, L.W. Tsay, J.J. Kai, The oxidation behavior of an equimolar FeCoNiCrMn high-entropy alloy at 950 °C in various oxygen-containing atmospheres, Corros Sci. 108 (2016) 209-214. https://doi.org/10.1016/j.corsci.2016.03.020.

[34] F.H. Stott, F.I. Wei, C.A. Enahoro, The influence of manganese on the High-temperature oxidation of iron-chromium alloys, Corrosion and Materials. 40(4) (1989) 198-205. https://doi.org/10.1002/maco.19890400403.

[35] R.K. Wild, High temperature oxidation of austenitic stainless steel in low oxygen pressure, Corros Sci. 17(2) (1977) 87-104. https://doi.org/https://doi.org/10.1016/0010-938X(77)90011-7.

[36] G. Laplanche, U.F. Volkert, G. Eggeler, E.P. George, Oxidation Behavior of the CrMnFeCoNi High-Entropy Alloy, Oxid Met. 85(5-6) (2016) 629-645. https://doi.org/10.1007/s11085-016-9616-1.

[37] Y.K. Kim, Y.A. Joo, H.S. Kim, K.A. Lee, High temperature oxidation behavior of Cr-Mn-Fe-Co-Ni high entropy alloy, Intermetallics. 98 (2018) 45-53. https://doi.org/10.1016/j.intermet.2018.04.006.

[38] D.J. Young, B.A. Pint, Chromium volatilization rates from $Cr_2O_3$ scales into flowing gases containing water vapor, Oxid Met. 66(3-4) (2006) 137-153. https://doi.org/10.1007/s11085-006-9030-1.

[39] T. Perez, L. Latu-Romain, R. Podor, J. Lautru, Y. Parsa, S. Mathieu, M. Vilasi, Y. Wouters, In situ oxide growth characterization of Mn-containing Ni-25Cr (wt%) model alloys at 1050 °C, Oxid Met. 89(5-6) (2017) 781-795. https://doi.org/10.1007/s11085-017-9819-0.

[40] C. Liu, X. Jiang, H. Sun, Y. Zhang, Y. Fang, R. Shu, Microstructure and mechanical properties of bioinspired laminated CoCrFeNiMn high entropy alloy matrix composites reinforced with graphene, Mat Sci Eng A-Struct. 859 (2022). https://doi.org/10.1016/j.msea.2022.144198.

[41] R. Shu, X. Jiang, H. Sun, Z. Shao, T. Song, Z. Luo, Recent researches of the bio-inspired nano-carbon reinforced metal matrix composites, Compos Part A-Appl S. 131 (2020). https://doi.org/10.1016/j.compositesa.2020.105816.

[42] G. Xu, K. Wang, H. Li, J. Ju, X. Dong, H. Jiang, Q. Wang, W. Ding, In situ nanoparticle-induced anti-oxidation mechanisms: Application to FeCrB alloys, Corros Sci. 190 (2021). https://doi.org/10.1016/j.corsci.2021.109656.

[43] Y. Pan, X. Lu, M.D. Hayat, F. Yang, C. Liu, Y. Li, X. Li, W. Xu, X. Qu, P. Cao, Effect of Sn addition on the high-temperature oxidation behavior of high Nb-containing TiAl alloys, Corros Sci. 166 (2020). https://doi.org/10.1016/j.corsci.2020.108449.

[44] N.K. Adomako, J.H. Kim, Y.T. Hyun, High-temperature oxidation behaviour of low-entropy alloy to medium- and high-entropy alloys, J Therm Anal Calorim. 133(1) (2018) 13-26. https://doi.org/10.1007/s10973-018-6963-y.

[45] F. Ye, Z. Jiao, Y. Yang, Effect of medium temperature precipitation phase and Mn element diffusion mechanism on high temperature oxidation process of repair and remanufacture CoCrFeMnNi high-entropy alloy cladding, Mater Res Express. 6(5) (2019). https://doi.org/10.1088/2053-1591/ab01be.

[46] B. Gleeson, D.L. Douglass, F. Gesmundo, The sulfidation behavior of Co-Mo alloys containing various ternary additions, Oxid Met. 34(1) (1990) 123-150. https://doi.org/10.1007/BF00664342.

[47] R.E. Lobnig, H.P. Schmidt, K. Hennesen, H.J. Grabke, Diffusion of cations in chromia layers grown on iron-base alloys, Oxid Met. 37(1) (1992) 81-93. https://doi.org/10.1007/BF00665632.

[48] A. Ferrari, F. Körmann, Surface segregation in Cr-Mn-Fe-Co-Ni high entropy alloys, Appl Surf Sci. 533 (2020). https://doi.org/10.1016/j.apsusc.2020.147471.

[49] K.Y. Tsai, M.H. Tsai, J.W. Yeh, Sluggish diffusion in Co-Cr-Fe-Mn-Ni high-entropy alloys, Acta Mater. 61(13) (2013) 4887-4897. https://doi.org/10.1016/j.actamat.2013.04.058.

[50] D. Gaertner, J. Kottke, G. Wilde, S.V. Divinski, Y. Chumlyakov, Tracer diffusion in single crystalline CoCrFeNi and CoCrFeMnNi high entropy alloys, J Mater Res. 33(19) (2018) 3184-3191. https://doi.org/10.1557/jmr.2018.162.

[51] Y.J. Li, A. Savan, A. Kostka, H.S. Stein, A. Ludwig, Accelerated atomic-scale exploration of phase evolution in compositionally complex materials, Mater Horiz. 5(1) (2018) 86-92. https://doi.org/10.1039/c7mh00486a.

[52] J.Y. He, H. Wang, Y. Wu, X.J. Liu, T.G. Nieh, Z.P. Lu, High-temperature plastic flow of a precipitation-hardened FeCoNiCr high entropy alloy, Mat Sci Eng A-Struct. 686 (2017) 34-40. https://doi.org/10.1016/j.msea.2017.01.027.

[53] A.Z. Hed, D.S. Tannhauser, Contribution to the Mn‐O phase diagram at high temperature, J Electrochem Soc. 114(4) (1967) 314. https://doi.org/10.1149/1.2426584.

[54] Y. Garip, O. Ozdemir, Comparative study of the oxidation and hot corrosion behaviors of TiAl-Cr intermetallic alloy produced by electric current activated sintering, J Alloy Compd. 780 (2019) 364-377. https://doi.org/10.1016/j.jallcom.2018.11.324.

[55] A. Shaga, P. Shen, L.-G. Xiao, R.-F. Guo, Y.-B. Liu, Q.-C. Jiang, High damage-tolerance bio-inspired ZL205A/SiC composites with a lamellar-interpenetrated structure, Mat Sci Eng A-Struct. 708 (2017) 199-207. https://doi.org/10.1016/j.msea.2017.09.114.

[56] J. Liu, D.-B. Xiong, Z. Tan, G. Fan, Q. Guo, Y. Su, Z. Li, D. Zhang, Enhanced mechanical properties and high electrical conductivity in multiwalled carbon nanotubes reinforced copper matrix nanolaminated composites, Mat Sci Eng A-Struct. 729 (2018) 452-457. https://doi.org/10.1016/j.msea.2018.05.091.

[57] X. Chen, J. Tao, J. Yi, Y. Liu, C. Li, R. Bao, Strengthening behavior of carbon nanotube-graphene hybrids in copper matrix composites, Mat Sci Eng A-Struct. 718 (2018) 427-436. https://doi.org/10.1016/j.msea.2018.02.006.

[58] D.B. Xiong, M. Cao, Q. Guo, Z. Tan, G. Fan, Z. Li, D. Zhang, Graphene-and-Copper artificial nacre fabricated by a preform impregnation process: Bioinspired strategy for strengthening-toughening of metal matrix composite, ACS Nano. 9(7) (2015) 6934-6943. https://doi.org/10.1021/acsnano.5b01067.

[59] E.J. Kautz, S.V. Lambeets, D.E. Perea, A.Y. Gerard, J. Han, J.R. Scully, J.E. Saal, D.K. Schreiber, Element redistributions during early stages of oxidation in a $Ni_{38}Cr_{22}Fe_{20}Mn_{10}Co_{10}$ multi-principal element alloy, Scripta Mater. 194 (2021). https://doi.org/10.1016/j.scriptamat.2020.10.051.